Intergranular corrosion: Comparison between experiments and cellular automata

Simone Guiso, Dung Di Caprio, Jacques de Lamare, B. Gwinner

To cite this version:

Simone Guiso, Dung Di Caprio, Jacques de Lamare, B. Gwinner. Intergranular corrosion: Comparison between experiments and cellular automata. Corrosion Science, 2020, 177, pp.108953. ⟨10.1016/j.corsci.2020.108953⟩. ⟨hal-02960051⟩

HAL Id: hal-02960051

https://hal.science/hal-02960051v1

Submitted on 7 Oct 2020

Intergranular corrosion: comparison between experiments and cellular automata

Simone Guiso[a,b], Dung di Caprio[a], Jacques de Lamare[b,*], Benoît Gwinner[b]

[a] *Chimie ParisTech, PSL Research University, CNRS, Institut de Recherche de Chimie Paris (IRCP), F-75005 Paris, France*
[b] *Des-Service de la Corrosion et du Comportement des Matériaux dans leur Environnement (SCCME), CEA, Université Paris-Saclay, F-91191, Gif-sur-Yvette, France*

Abstract

In this paper, a 3D cellular automata approach of intergranular corrosion in presented. A model is proposed, along with experimental results both qualitatively (groove morphology, groove angle distribution) and quantitatively (mass loss, corrosion rate, corrosion front evolution). Simulations have been performed using a new asynchronous algorithm: the choice of the most adequate grid is also discussed. The model investigates the statistical variation of the corrosion front and provides useful information to make predictions on material ageing.

Keywords: intergranular corrosion, cellular automata, modelling, material ageing, stainless steel

---

1. Introduction

In France, the PUREX (Plutonium and Uranium Refining by EXtraction) process is used to reprocess spent fuel in a nuclear fuel cycle [1]. The process involves the treatment of the spent fuel in hot and concentrated nitric acid for liquid-liquid extraction of the recoverable material (uranium and plutonium). In some particular conditions, the interaction between the nitric media and the structural stainless steel (SS) may lead to intergranular corrosion (IGC) phenomena [1, 2, 3].

---

[*] Corresponding author
Email address: `jacques.de-lamare@cea.fr` (Jacques de Lamare)

Preprint submitted to Corrosion Science *October 7, 2020*

Understanding IGC is therefore crucial. This particular type of corrosion promotes grain detachment and leads to corrosion kinetics larger than expected. IGC study is a challenge that involves both experimental campaigns and simulation modelling.

Experimentally, IGC corrosion kinetics is mainly studied using weight-loss (WL) techniques and electrochemical measurements. However, experiments are intrinsically limited in duration and cannot always provide sufficient information to predict material behaviour over long time periods. Modelling can then provide an important support.

The way IGC finds its path along grain boundaries is essential to understand IGC corrosion kinetics and may lead to different characteristic morphologies in relation to grain detachment. Thus, on the modelling side, different paths have been recently investigated, where focus is on the evolution of the corrosion morphology. In brick-wall models [4], the IGC penetration is described as a function of the probability of choosing a defined path in a "wall structure". Monte-Carlo simulations were performed by Lim et al. [5] to estimate the average IGC penetration depth at precise time steps in comparison with experimental tests. A stochastic reduced order model (SROM) was instead proposed by Sarkar et al. [6] to quantify the uncertainty on IGC rates. Results demonstrate that this approach is more suitable than MC method for this purpose.

Despite all these achievements, the IGC kinetics is yet to be fully understood. In particular, more investigations should be addressed to the morphology characterization of the IGC grooves and to their progression inside the material, which is difficult to access experimentally. A complete description of the phenomenon would be an important tool for the industry in strong need of predictive models for material ageing. The objective of this study is to start filling this gap by presenting a predictive tool for material ageing that includes a fine description of the material morphology evolution. In this paper, the study is focused on "non-sensitized" SS. A 3D stochastic CA model is presented and compared with some experimental tests already published [7, 8].

The paper is organized as follows: a brief background to the IGC study is presented in Section 2, followed by a description of the experimental tests in Section 3, and of the CA model in Section 4, while results are discussed in Section 5. The conclusive remarks are then presented in Section 6. Tables of symbols, abbreviations and references are provided at the end.

2. Background

From the experimental point of view, IGC has been studied in terms of WL measures. Specimens are usually exposed to a corrosive solution and extracted at precise time steps [7, 9]. The goal is to obtain information on mass loss and corrosion rate as a function of time.

In parallel, electrochemical tests are also performed to evaluate the risk of IGC. More generally, electrochemical measurements are classically used to characterize different aspects of the SS corrosion. For example, the determination of the pitting potential defines the sensitivity to this type of corrosion [10], double loop electrochemical potentiokinetic reaction tests inquire about the degree of sensitization of the SS [11], electrochemical impedance spectroscopy experiments give information on the limiting corrosion processes [12]. Among those, linear voltammetry is often performed in the case of IGC to investigate whether the SS remains passive (where the SS dissolves slowly and uniformly) or it is polarized in its transpassive state (where IGC occurs) in its chemical environment (see Figure 1) [13, 14].

In order to resist corrosion, the SSs used for structural material are screened in view of their corrosion resistance, optimized and qualified before their use. In particular, austenitic SSs with low carbon, high chromium and controlled silicon and phosphorus contents are preferred [15]. A stable passive layer protects all these materials so that corrosion, in normal conditions, is slow and uniform. However, too oxidizing conditions (e.g. nitric media containing oxidizing ions at high temperature like Vanadium (V)) may promote the deterioration of this passive layer and generate IGC phenomena. In this case, the cathodic reaction (reduction reaction) is fast and can lead to a shift of the corrosion potential to

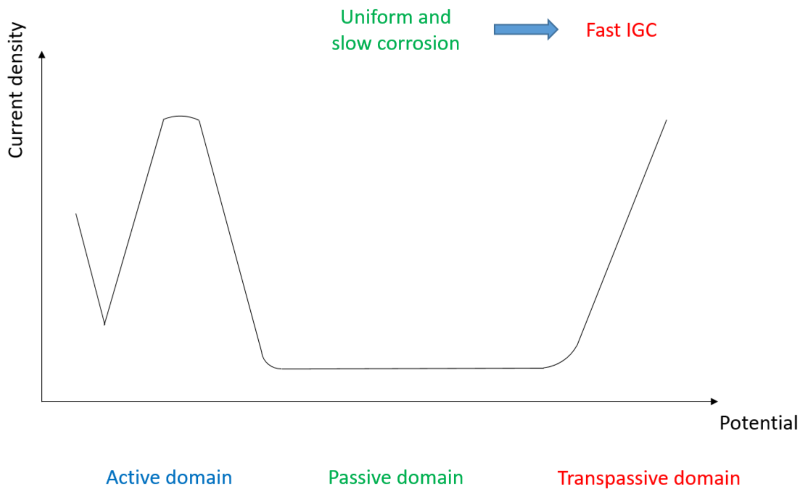

Figure 1: Simplified scheme of the different electrochemical domains.

the transpassive domain, thus exposing materials to IGC attack, as presented in Figure 1.

Normally, grain boundaries (GB) represent barriers that confer strength to metallic materials. However, in some environmental conditions, they are the main source of weakness and failures. Grain boundary degradation includes corrosion, cracking, embrittlement and fractures. According to literature [7, 16] two cases of IGC can be distinguished.

The first one includes the "sensitized" SSs, which present a relatively high carbon content. When SSs are subjected to long heat treatments at high temperatures (for instance, between 500 and 800°C), Cr and C species may diffuse through the material and precipitate as chromium carbides ($Cr_{23}C_6$) at grain boundaries. As chromium slowly diffuses from the grain matrix, a poor-in-chromium-content region is generated adjacent to $Cr_{23}C_6$ precipitates. In this region, the chromium content is not sufficient to provide a stable passive film to protect the SS. As a consequence, the SS is exposed to IGC attack [16]. To prevent these phenomena, different countermeasures have been considered. In the industrial field, for example, titanium (Ti) or niobium (Nb) are added to the material. Their presence in the matrix promotes the formation of Ti_xC or Nb_xC precipitates and prevents the formation of chromium carbides. Thus, the material maintains its passive layer - rich in chromium - and IGC attacks are avoided [17, 18].

As an alternative, the carbon content in SS may be reduced in order for it to be lower than 0.03 wt.% [16]. In this case, the carbon is soluble in the austenitic structure and it remains uniformly distributed in the crystal structure. The SS is then called "non-sensitized" and chromium carbides formation is avoided during high temperature treatments. However, IGC can still occur in some specific conditions. In the context of investigations on the corrosion behavior of a SS in a spent fuel reprocessing plant [1], experimental tests showed that the material can still be affected by IGC in presence of highly oxidizing media. The degradation of a non-sensitized SS is characterized by the formation of triangular grooves at grain boundaries (as represented in Figure 2). The progression of the grooves in the material bulk may cause grain detachment with a certain periodicity, as shown in Figure 3.

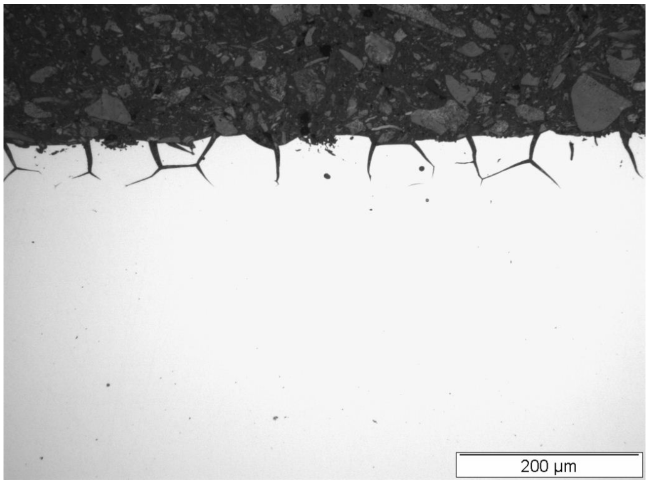

Figure 2: Cross section of a "non-sensitized" 310L SS suffering IGC [7].

On the modelling side, as already stated in the introduction, different paths

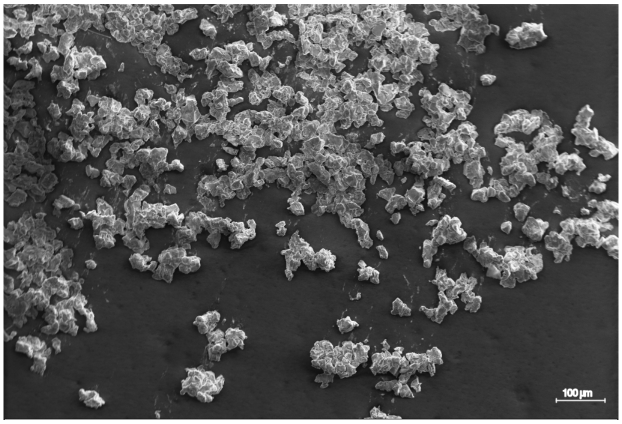

Figure 3: Scanning Electron Microscope observation of detached grains of a "non-sensitized" 304L SS [8].

have been recently investigated, among those a promising method is to model IGC phenomena through the cellular automata (CA) approach [19]. It consists of a dynamical system where both space and time are discretized [20, 21]. Each site (named cell) is identified by a state (defined from a finite list of possible states) and its spatial coordinates. The dynamics of the system is then regulated by a list of transition rules, which take into account the interaction between neighbouring cells (generally first-neighbour cells) [22].

Recently, different studies have been performed within this approach. Lishchuk et al. [23] improved their previous model [24] by developing a 3D stochastic CA model. A similar result was obtained by Jahns et al. [25] who, on the other hand, developed a 2D CA model to study the intergranular oxidation phenomenon. Igarashi et al. [26, 27] also focused their studies on the development of a 2D CA model to study IGC in stainless steels, while Di Caprio et al. [19] developed a 3D stochastic CA model to study IGC, by improving the previous 2D model [28].

Gwinner et al. [7, 29] proposed a phenomenological geometrical model to estimate the long-term corrosion rate of "non-sensitized" SS suffering IGC. The model assumptions are based on experimental observations: grooves grow symmetrically along the grain boundaries, groove angles are constant with time during IGC evolution and the groove depth is nearly homogeneous along the surface. Similar observations were obtained by Beaunier et al. [30], which proposed to describe IGC with two principal parameters:

- V_{gb} which represents the grain boundary dissolution rate
- V_s which represents the grain dissolution rate

The different approaches are summarized in the following Table 1 and 2, along with their main characteristics.

Table 1: Summary of the different IGC models with their main features

Model	**Approach**	**Results**
Brick-wall [4]	2D, probabilistic	• Minimum IGC path length as a function of time • Comparison with experimental results
Monte-Carlo [5]	3D, probabilistic	• Comparison with experimental results • IGC damage depth as a function of the degree of sensitiveness and of time
SROM [6]	1D, mathematical and probabilistic model	• Comparison SROM/Monte-Carlo simulations • Effect of the uncertainty in anodic/cathodic sites on the current density • Effect of the domain length on the current
Geometrical model [7, 29]	2D/3D, deterministic	• Groove angular description • Comparison with experimental results • Corrosion depth and corrosion rate

Table 2: Summary of the different CA IGC models with their main features

Reference	**Approach**	**CA grid / cell geometry**	**Results**
[23]	2D, probabilistic	Cubic / cubic 2D: 1216 cells/grain 3D: 448000 cells/grain	• Comparison with experimental results • Corrosion depth, path length
[24]	3D, probabilistic	Cubic / cubic 3D: 448000 cells/grain	• Comparison with experimental results • Corrosion depth, path length
[25]	2D, probabilistic	Square / Square Hexagonal grains	• Corrosion path • Comparison with experimental results (only microstructure)
[26, 27]	2D, probabilistic	Square / square Grain size randomly distributed	• Comparison with experimental results • Corrosion width and depth, corrosion rate
[19]	3D, probabilistic	Cubic / cubic Grain size randomly distributed	• Corrosion depth and corrosion rate • Roughness study
[28]	2D, probabilistic	Square / square Various types of grains and spatial distributions	• Evolution of the corrosion front as a function of different spatial arrangements (square, brick-wall, polygonal) • Surface roughness profile • Corrosion rate

3. Determination of the experimental corrosion velocities

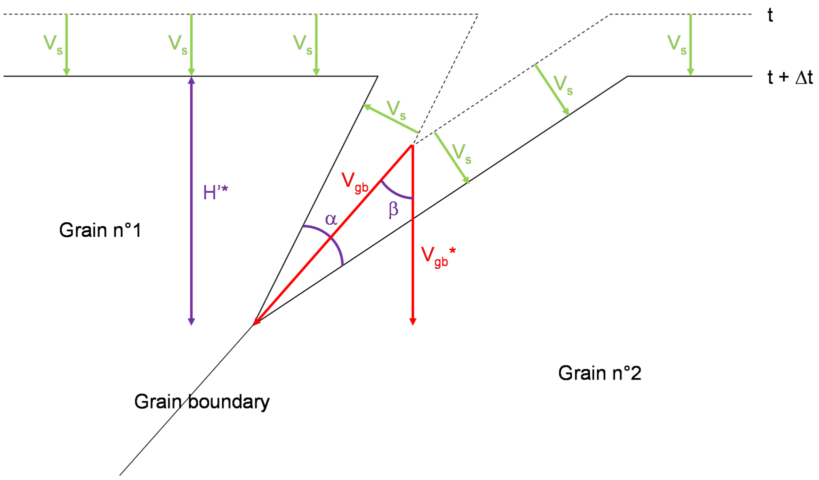

Figure 4: Schematic representation of the corrosion rates (V_{gb} and V_s, where $V_{gb} > V_s$), the groove depth ($H^{'*}$), the groove angle (α) and the groove inclination (β) [7].

Experimental tests were performed by Gwinner et al. [7] on an AISI 310L stainless steel. It presents a low carbon content and was firstly thermally treated (homogenization treatment and quenching) to avoid precipitate formation that would have brought a type of IGC proper to sensitized SS (see Section 2). The SS was exposed to a solution of nitric acid (HNO_3), containing an oxidizing ion (VO_2^+) at boiling temperature, that was renewed after each corrosion period of 160 h. SS specimens were periodically removed and examined. The experimental equivalent thickness loss (ETL_{exp}, in μm) was evaluated with the following relation

$$ETL_{\exp}(t) = \frac{m(t)}{\rho S} 10^4 \tag{1}$$

where $m(t)$ is the cumulated mass loss (in g) at time t, ρ is the SS density (8 g.cm^{-3}) and S is the initial surface of the polished sample (in cm^2) that is in contact with the corrosive agent. The instantaneous experimental corrosion rate CR_{exp} is then defined as

$$CR_{\mathrm{exp}}\left(t+\frac{\Delta t}{2}\right)=\frac{ETL_{\mathrm{exp}}\left(t+\Delta t\right)-ETL_{\mathrm{exp}}\left(t\right)}{\Delta t} \tag{2}$$

where Δt is the duration of a corrosion period between two mass loss measurements.

Besides the experimental tests, a semi-empirical model was also developed to estimate the long term IGC evolution for the SS [7]. According to this model, a triangular groove is represented as in Figure 4.

The model is based on experimental observations of the mass loss kinetics. According to experimental data, the corrosion rate (V_{corr}) linearly evolves from an initial value to a steady-state condition. The initial value corresponds to the metal dissolution at the initial state (t=0), whose value is V_s. The steady-state value corresponds to the corrosion rate at which the IGC kinetics is fully controlled by grain dropping: in this case, the corrosion rate is equal to V_{gb}^*. As discussed in [7], the transition time from the linear trend to the steady-state condition is estimated (in good agreement with the experimental observations) to be at $t=1.5\,\frac{D}{V_{gb}^*}$, where D is the average grain dimension.
Following these assumptions, the corrosion rate (V_{corr}) can be expressed as:

$$t\leq 1.5\,\frac{D}{V_{gb}^*},\qquad V_{corr} = \frac{2}{3}\frac{V_{gb}^*}{D}\left(V_{gb}^*-V_s\right)t+V_s \tag{3}$$

$$t\geq 1.5\,\frac{D}{V_{gb}^*},\qquad V_{corr} = V_{gb}^* \tag{4}$$

V_s and V_{gb}^* are then obtained by fitting the first 4 points of the experimental corrosion rate kinetics with the linear trend of the semi-empirical model.
V_{gb} is then determined by the following formula:

$$V_{gb}=\frac{{V_{gb}}^*}{\cos(\beta)} \tag{5}$$

where β is defined in Figure 4 and averaged over different grooves [7].

In [7], $V_s=92\mu$m/y, $V_{gb}^*=1287\mu$m/y and $\beta=35^\circ$ have been obtained.

4. 3D Cellular automata model

The 3D stochastic CA model will hereafter be presented. The methodology belongs to the so-called "grey-box" class of approaches as it stands between "black-box" and "white-box" models: the former are phenomenological approaches where the model response is directly related to input data but no interpretation nor mechanistic description is introduced; the latter are based on a detailed understanding of physical laws and processes, but are too complex to be implemented. The CA model presented in this paper adopts a simple stochastic mesoscopic level of description. The main features of the model are those who characterize the CA approach: a lattice grid, a list of possible cell states, the corrosion rules. The model is then related to "real" space-time quantities by providing space and time scales. Finally, the construction of the Voronoï diagram, used to model the granular microstructure of the material, is detailed.

4.1. Cell states, corrosion rules and probabilities

The CA model is made of a grid of cells that can acquire three possible chemical states: IGN, which represents the grain boundaries, GRN that represents the grains and SOL that defines the corrosive agent.

At each iteration i, CA cells can change their state according to the transition rules. In the case of the corrosion process, IGN and GRN cells change their states to SOL according to two effective probabilities, P'_{ign} for grain boundaries and P'_{grn} for grains, as presented in Figure 5. When a SOL cell comes into contact with a GRN cell (or IGN cell), a random number δ is drawn and compared to a probability P'_{grn} (or P'_{ign}) associated to the cell according to the following equations

$$P'_{grn} = P_{grn} \frac{N_b}{N_{b,max}} \tag{6a}$$

$$P'_{ign} = P_{ign} \frac{N_b}{N_{b,max}} \tag{6b}$$

where P_{grn} and P_{ign} are the intrinsic corrosion probabilities for the GRN and IGN cells. The ratio $\frac{N_b}{N_{b,max}}$ is a correction related to the cell environment,

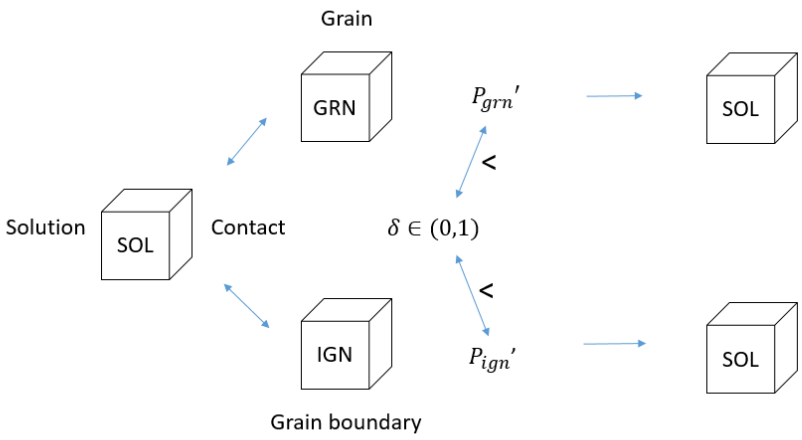

Figure 5: Schematic representation of the corrosion probabilistic transition rule.

where N_b is the number of SOL cells in contact with the considered GRN (or IGN) cell and $N_{b,max}$ is the maximum possible number of SOL cells in contact with a single cell.
If $\delta < P'_{grn}$ (similarly $\delta < P'_{ign}$), the cell will change its state to SOL, i.e. the cell is "corroded", otherwise it keeps its state (and the cell is not "corroded"). In this CA model at mesoscopic scale, the goal of Eq. (6a) and (6b) is to represent the fact that the more SOL cells surround a GRN (or an IGN) cell, the faster corrosion is. The lifetime of a cell is assumed to be directly proportional to the number of surrounding SOL cells, considering the fact that dissolution is proportional to the surface in contact with the solution. This feature is new in such a type of model.

In order to compare the model to experimental data, the choice of both intrinsic corrosion probabilities P_{grn} and P_{ign} is crucial. A preliminary study of pure grain dissolution is firstly performed to assess the functional relation between probabilities and corrosion velocity in the simulation. A system with a single 3D block of GRN cells surrounded by three layers of SOL cells is adopted. The precise number of SOL layers is in fact immaterial as long as all GRN top plane cells are in contact with at least a SOL cell. In this study, the P_{grn}

probability is then varied. Following the results in [31], a hexagonal close-packed (HCP) grid is chosen for this preliminary study.

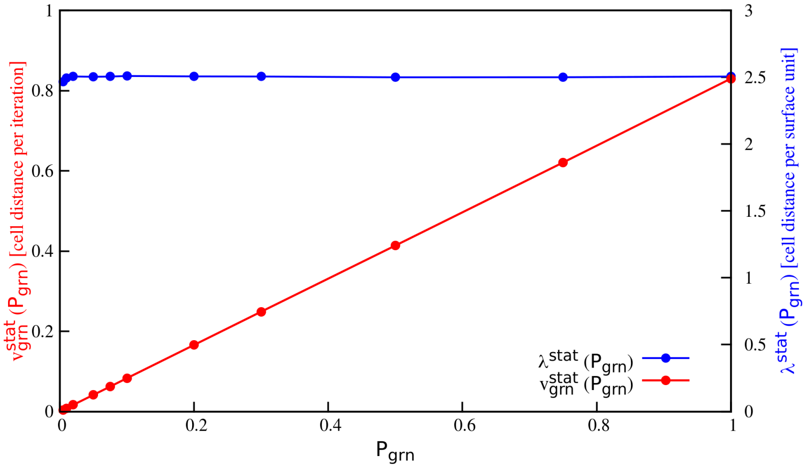

Figure 6: Grain dissolution velocity v_{grn}^{stat} and chemical roughness λ^{stat} in stationary regime as function of the grain corrosion probability P_{grn}.

In Figure 6, the results of the study are presented in terms of corrosion velocity $v_{grn}^{stat}(P_{grn})$ (expressed as the number of GRN cells dissolved per iterations per cell in the horizontal plane) and chemical roughness $\lambda^{stat}(P_{grn})$, as a function of P_{grn} in stationary conditions. The chemical roughness, also known as rugosity in some domains, is the number of GRN cells in contact with at least one SOL cell, normalized with respect to the horizontal surface of the system. This quantity is of interest because it is directly related to the reactivity of the surface, as it gives information on the kinetics. This contrasts with the standard physical roughness (generally defined as the root mean square of the deviation of the profile with respect to the mean height) that is more a morphological information. Note also that the physical roughness increases as a power law with time; a stationary regime is reached only due to finite size effects which limit the power law. Corrosion velocity and chemical roughness are averaged between the iteration n, which indicates the beginning of the stationary regime, and iteration N, in such away that $N - n$ is a sufficiently large number of iterations for the average. Their expressions read as

$$v_{grn}^{stat}(P_{grn}) = \frac{1}{N_{XY}} \frac{N_{grn}(n) - N_{grn}(N)}{N - n} \tag{7}$$

$$\lambda(P_{grn}) = \frac{1}{N_{XY}} \sum_{i=n}^{N} \frac{N_{grn-sol}(i)}{N - n} \tag{8}$$

where $N_{grn}(i)$ is the number of GRN cells that are still present in the system after i iterations and $N_{grn-sol}(i)$ is the number of GRN cells that are in contact with at least one SOL cell at the iteration i, N_{XY} is the total number of cells that are present in a horizontal XY-plane.

Figure 6 shows that the velocity is a linear function of P_{grn} and that the chemical roughness remains constant with P_{grn}.

Figure 7 shows another characterisation of the surface: the percentage histogram of the number of SOL neighbours for the GRN cells on the surface. Such information is relevant as the probabilities (Eq. (6a) and (6b)) depend on the number of neighbours to a cell. The statistical distribution of all SOL neighbours is shown to remain identical whatever the value of P_{grn}.

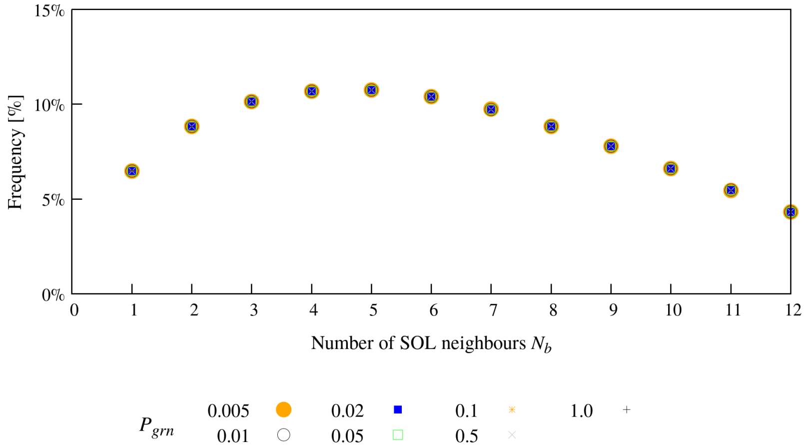

Figure 7: Distribution of the number N_b of SOL neighbours to GRN cells during grain dissolution for different values of P_{grn}.

The results above are important in order to set the relations between simulated and experimental quantities and allow the comparison between the two. The linearity of the corrosion velocity with P_{grn} indicates that changing P_{grn} is equivalent to scaling the real time duration of a simulation iteration. This means that, in order to represent a given corrosion rate, one can first associate a simulation iteration i to a given time duration and then tune the value of P_{grn} to obtain the experimental corrosion rate. However, owing to linearity, there is not one sole choice. The same process can be represented by increasing the duration of an iteration (for instance multiplying it by a given coefficient) and correlatively decreasing P_{grn} (that is dividing it by the same coefficient). Note that, alternatively, it is possible to choose P_{grn} and the iteration time step in accordance to the corrosion rate. In all cases, the system is the same and the quantity of dissolved material per real time units remains unchanged. If the described system is identical, the chemical roughness and the SOL neighbours distribution remain unchanged, independently of P_{grn}: which is indeed what has been proved in the simulations.

Note that the linearity between corrosion rate and probabilities is not evident, as not all algorithms provide such property. In this paper, this property is a consequence of the asynchronous algorithm (Figure 5), where cell states are updated in the order as they come along during simulations. The standard synchronous algorithm (where all lattice cells updating is performed simultaneously), that was chosen in [31], does not exhibit linearity between corrosion velocity and P_{grn} for all values. A synchronous algorithm was also used in a previous IGC study in [19].

An important consequence of the linearity of the corrosion rate with P_{grn}, is that it is possible to model a given $\frac{v_{grn}}{v_{ign}}$ velocity ratio using an identical $\frac{P_{grn}}{P_{ign}}$ probability ratio.

In conclusion, the two CA corrosion probabilities (P_{grn} and P_{ign}) are chosen as follows. To achieve faster simulations, the highest probability is associated to the fastest process. Adopting a smaller value is less efficient as some iterations do not lead to a IGN dissolution event. The IGN corrosion probability P_{ign}

is set equal to 1. Then, P_{grn} is set in order to have $\frac{P_{grn}}{P_{ign}}$ ratio equal to the experimental ratio $\frac{v_{grn}}{v_{ign}}$, which in this case corresponds to $\frac{V_s}{V_{gb}} \approx 0.0581$ (see §3).

4.2. Grid

The choice of an appropriate grid is important to best describe the behaviour of a material. The specific kinetics of IGN corrosion is related to the crystallographic misorientation of adjacent grains and to the chemical composition of these regions. GB are schematically represented as planes and do not have a preferential spatial orientation. Therefore any realistic model must statistically reproduce GB corrosion velocities, which are isotropic and independent on the planar GB spatial orientation. Dealing with CA approach means that simulations are performed on discrete lattices, which therefore are intrinsically anisotropic. A recent study [31] aimed at finding the best suited lattice to get as close as possible to an isotropic behaviour. It showed that the HCP grid is the closest to an "isotropic" grid in view of IGC corrosion along grain boundaries. However, this study was performed using a synchronous algorithm, which has been here substituted by an asynchronous algorithm. The purpose of this section is to investigate whether an identical statement can be valuable with the present asynchronous algorithm.

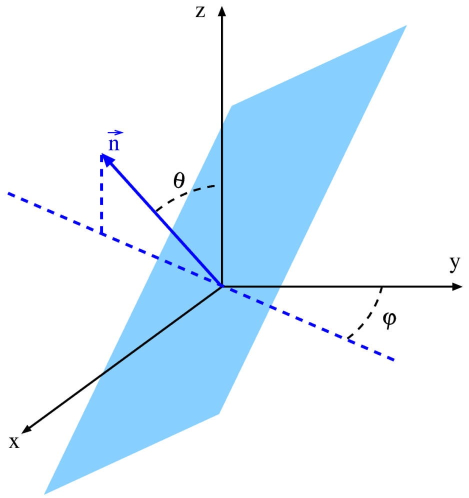

Figure 8: Schematic 3D view of a planar GB (in blue) defined by its polar and azimuthal angles $(\theta,\,\varphi)$ and its normal $\vec{n}$ [31].

The isotropy performance of the model (grid and algorithm) is estimated by calculating the relative deviation $\varepsilon\left(\theta,\varphi\right)$ of the simulated IGN corrosion velocity with respect to the theoretical (purely isotropic) case

$$\varepsilon\left(\theta,\varphi\right)=\frac{v_{ign}^{z,sim}-v_{ign}^{z,th}}{v_{ign}^{z,th}} \tag{9}$$

where $v_{ign}^{z,sim}$ is the simulated vertical component of the velocity, $v_{ign}^{z,th}=sin(\theta)$ is the vertical component of the reference isotropic velocity and $(\theta,\ \varphi)$ are the polar coordinates of the grain boundary, as shown in Figure 8. The corrosion probability is here $P_{ign}=1$.

As in the previous case, the HCP grid has been chosen. A top view of the grid is presented in Figure 9. Keep in mind that in this grid each cell has 12 neighbouring cells at equal distance, subdivided as follows: 6 cells in the same horizontal plane, 3 cells in the plane directly above and 3 cells in the plane below. An identical spatial layout is repeated every two horizontal planes (ABAB... structure).

The angular distribution of the velocity in the HCP grid is presented in Figure 10 in terms of $\delta\left(\theta,\varphi\right)=\varepsilon\left(\theta,\varphi\right)-\overline{\varepsilon}$, where $\overline{\varepsilon}$ is the average of $\varepsilon\left(\theta,\varphi\right)$ over

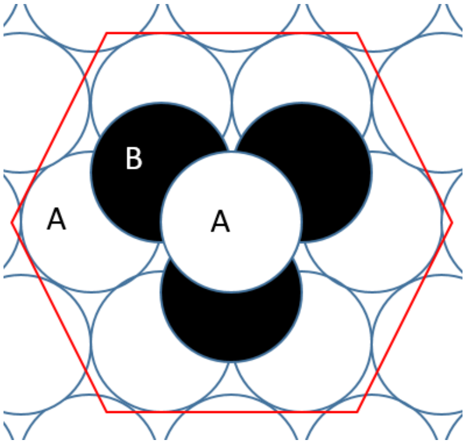

Figure 9: Schematic representation of the HCP grid, with the representation of the vertical cell stacking.

different (θ, φ) orientations: θ varies between 10° and 90°, and φ between 0 and 355°, each of them every 5°. Results are averaged over four different simulation data generated with four different random seeds. For a grain boundary thickness of two cells, the average deviation $\overline{\varepsilon}$ is equal to -2.05%, which indicates that simulation velocity is slightly lower than the theoretical one. The standard deviation is around 1.58%. Figure 10 shows that the deviation δ stands within 2%, except for particular angles at $\theta = 90°$ and $\varphi = 0$ [90°], which are characterized by a higher velocity ("red points" in the Figure). To understand these specificities, the layout of the grain boundaries for these particular angles was investigated in detail. It was found that the velocity increase is caused by a thickness effect, which occurs when the IGN plane is parallel to a grid face. In these geometries, despite an integer grain boundary thickness of two, the grain boundary of the HCP lattice appears to be constituted of a slab with an alternation of two and three cells thickness. In the model, the IGN dissolution probability (Eq. 6b) depends on the number of solution neighbours. A thickness larger than two in these directions causes an increase of the velocity. This effect was investigated by varying the GB slab thickness.

In Figure 11, two different orientations have been investigated, $(\theta, \varphi) =$

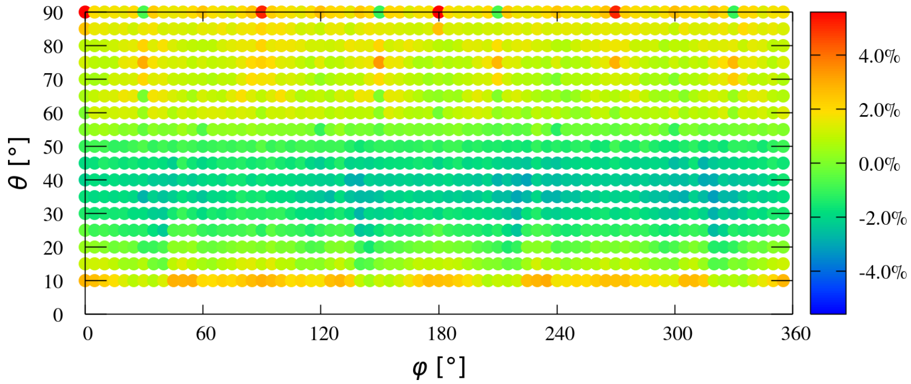

Figure 10: Simulated corrosion velocity results for HCP grid, expressed in terms of $\delta(\theta, \varphi)$ (in percentage colored scale).

$(90°, 0°)$ and $(90°, 30°)$. These orientations of the grain boundary correspond to the most extreme cases representing respectively the highest and the lowest velocities with respect to the average. For both orientations, the velocity is an increasing function of thickness. Such an outcome is expected since the probability (Eq. 6b) is an increasing function of the number of neighbours, which is larger when thickness increases. However, the velocity difference between the two orientations decreases when the thickness increases. This can be understood by the relative difference in thickness between $\varphi = 0°$ and $\varphi = 30°$ that decreases when the slab thickness increases. Note that results are averaged here over 50 different simulations: as a consequence, the error bars are small.

In conclusion, the relative small variations between the simulated and the theoretical velocity seen in Figure 10 for asynchronous algorithm confirm the result that was obtained for the synchronous algorithm in [31]: the HCP grid is then chosen for the comparison with the experimental data.

4.3. Space and time, CA to experiments conversion factors

A summary of the main parameters for the experimental setup and the corresponding CA simulations is presented in Table 3. The grain size within the CA model is set by the number of initial seeds N_{seed}, independently on the grain dimension in the "real" experimental case: in this case $N_{seed} = 104$. This

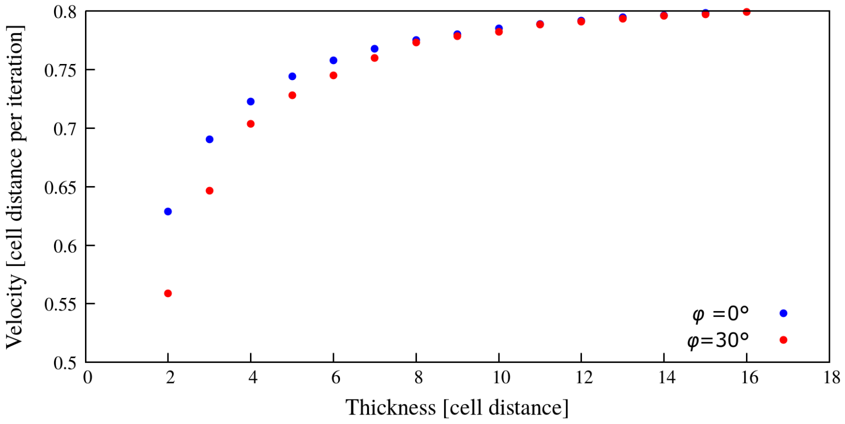

Figure 11: Simulated corrosion velocity as a function of the grain boundary thickness for two configurations: $(\theta, \varphi) = (90°, 0°)$ in blue and $(\theta, \varphi) = (90°, 30°)$ in red. Results are averaged over 50 different simulations.

value corresponds to a balance between having, within the simulation box, both sufficiently large grains and a sufficient number of grains in order to describe the corrosion progression in the material. The characteristic dimension of a grain is determined by the number of seeds with the following equation:

$$D_{sim} = \sqrt[3]{\frac{N_{xyz}}{N_{seeds}}} = 272 \tag{10}$$

where N_{xyz} is the total number of cells that are present in the system.

To compare experimental data and simulation results, it is necessary to associate the real space and time scales with CA dimensionless quantities. In the CA approach, these scales correspond respectively to the cell distance and to the duration of one iteration. At this point, two conversion factors need to be introduced.

The first coefficient is a space scaling factor A (in μm/cell), which can be calculated by the ratio between the experimental average grain dimension (in μm) [7] and the CA average grain dimension (in number of cells). In this case, $A = \frac{84}{272} \approx 0.309$ μm/cell.

Once the spatial scale is defined, the second coefficient is the time scaling factor B (in hour/iteration) that enables to convert the duration of a simulation

Table 3: Comparison between experimental and simulation main parameters.

Parameter	Experimental tests [7]	CA simulations
Dimension	$30 \times 20 \times 1.5$ mm^3	$1280 \times 1280 \times 1280$ cells
Average grain lateral dimension	84 μm	272 cells
Stationary vertical corrosion velocity	1206 ± 152 μm/y	0.446 ± 0.003 cell/iteration
Corrosion velocities/ probabilities	$v_{gb} = 1582.3 \pm 187$ μm/y, $v_s = 92 \pm 46$ μm/y	$P_{ign} = 1$, $P_{grn} \approx 0.0581$

step into "real" hours. It is calculated as the ratio between the stationary CA corrosion velocity and the experimental one. In this case, $B = 8760 \times \frac{0.446 \times 0.309}{1206} \approx 1.0$ hour/iteration, where an extra factor 8760 accounts for the change of time unit from years (used in corrosion velocity) to hours (used in the corrosion experiments). The coefficient A is also present because the ratio between experimental velocity and CA velocity involves a spatial ratio, with the space expressed once in μm and once in cells. Note that the specific value for B equal to 1 is not meaningful; it is a coincidence arisen from the experimental conditions and the chosen units.

4.4. Voronoï tessellation

The material microstructure has been reproduced through a Voronoï diagram [32, 33]. It consists of a partitioning of the 3D grid into regions originated by a set of starting points, called seeds. To build the Voronoï diagram, a spherical region is progressively grown around each seed along all directions: when two regions meet each other, a border is determined along the mediator plane. Then, each seed keeps growing in all directions until all grid cells become part of a region including a seed or a border. Note that periodic boundary conditions are applied by replicating the entire seed spatial distribution to complete the Voronoï structure at boundaries in all directions. Once the Voronoï tessellation is complete, states are assigned to cells: those which belong to borders assume the IGN state, the others the GRN state. This construction leads to grain boundaries with a precise two cells thickness, reducing the above-mentioned thickness velocity issue.

The initial grid is then obtained by assigning the SOL state to the three uppermost XY-layers: during dissolution, the solution path is conducted from the top of the grid to the bottom. Note that the top layer grain size distribution is different than the one in the bulk because the grains on the surface have been cut. An example of the initial grid is represented in Figure 12.

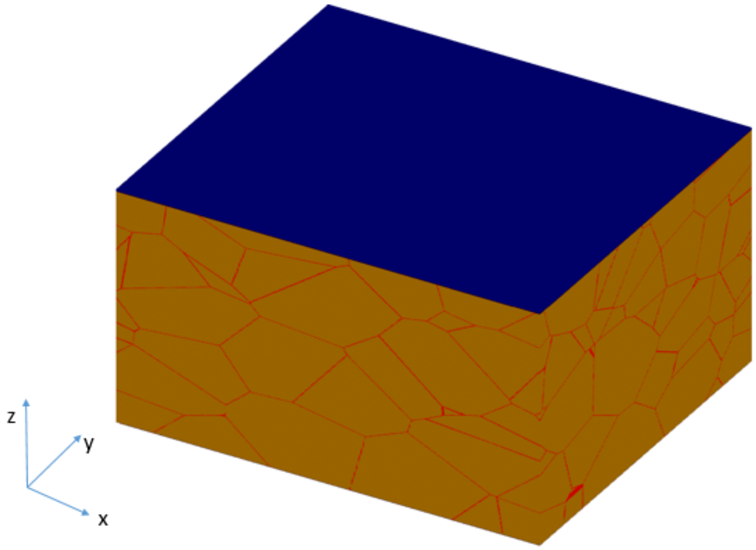

Figure 12: Representation of the 3D initial grid of IGC model.

4.5. Computational setup

The simulation code has been written in C language, in NVIDIA's CUDA environment, and simulations have been performed using NVIDIA Tesla K80 cards in Dell PowerEdge C4130 servers with Intel Xeon E5-2640 processors. A single simulation run takes from 24 to 48 hours, depending on the values that are given to P_{grn} and P_{ign} (the higher the values, the lower the simulation time). To obtain a reasonable statistics, results are averaged over 50 different Voronoï diagrams.

5. Results

5.1. Preliminary observations on the morphology

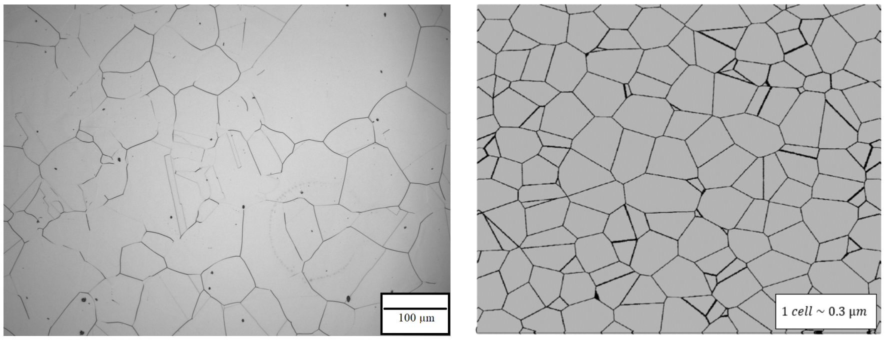

Figure 13: Microstructure before corrosion of AISI 310L stainless steel [7] (left) in comparison with a cut view of the Voronoï microstructure (right).

A comparison between a section of the experimental reference test specimen and a section of the 3D CA model is presented in Figure 13. Both structures of grains are similar, although some differences can be observed. Some grain boundaries are not clearly visible on the experimental image due to a lower reactivity of these grain boundaries during the metallographic etching process. Some crystal twinning appears on the experimental image, which are not modelled by CA. A majority of triple grain boundaries forming 120° angles suggests the structure is stabilized.

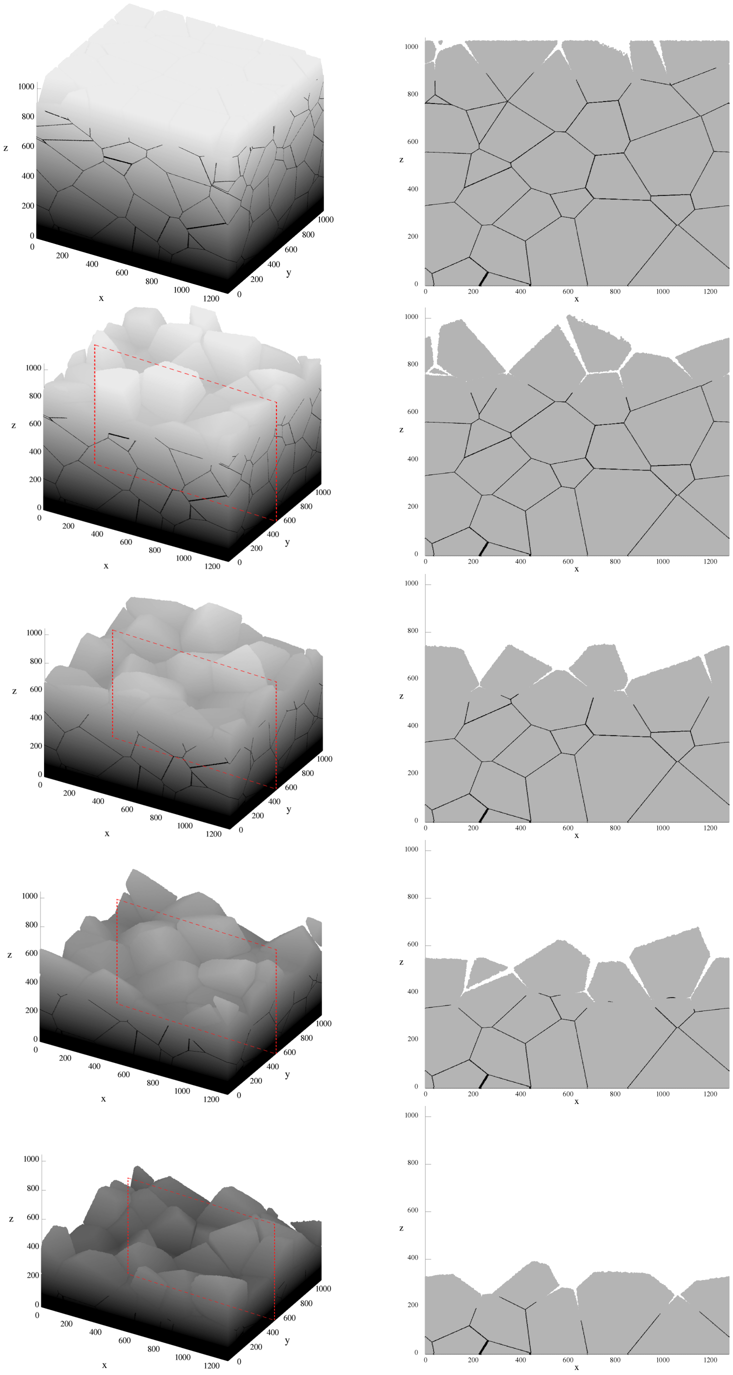

Figure 14: 3D views (left) and 2D sections for the planes indicated in red (on top) of the system at times $t = 400, 800, 1200, 1600, 2000$ h. Detached grains are removed for visibility.

Figure 14 shows 3D perspectives and 2D sections of CA simulations during corrosion at $t = 400, 800, 1200, 1600, 2000$ h. The groove progression inside the material is visible as well as the consequent grain detachment. Good qualitative agreement with experimental observations is found (cf. Figure 2). Some detached grains are presented in Figure 15, in comparison with Figure 3.

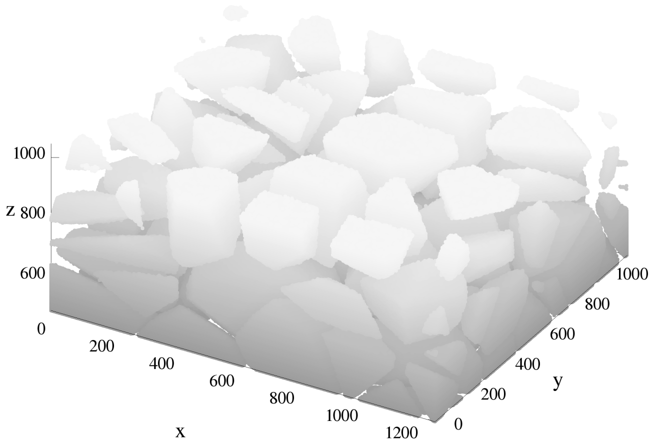

Figure 15: 3D view of some detached grains at t=1600 h.

Figure 16 shows the distribution of the α' angles, the α-projection observed along some 2D cross sections of the system for both experimental tests and CA simulations. Two "real" times, with the correspondent iterations, have been considered: the first one, t=641h, in the groove progression regime, while the second one, t=1602h, includes the groove progression and the grain detachment phenomena. CA α' angle distribution is an average over all α' angles that are observed in 2 equally spaced cross sections for 10 different simulations. In each section, 7 to 8 grooves were generally found.

Results confirm that, in both approaches, the distribution does not have a significant evolution in time. In the simulations, a narrow peak was found between 5° and 15°, similar to the experimental observations [7]. A comparison of the main results is presented in Table 4: the difference between experimental and CA average values of α' is within the standard deviation. A distribution tail for larger α' is observed. It is due to the fact that α' angles are obtained from

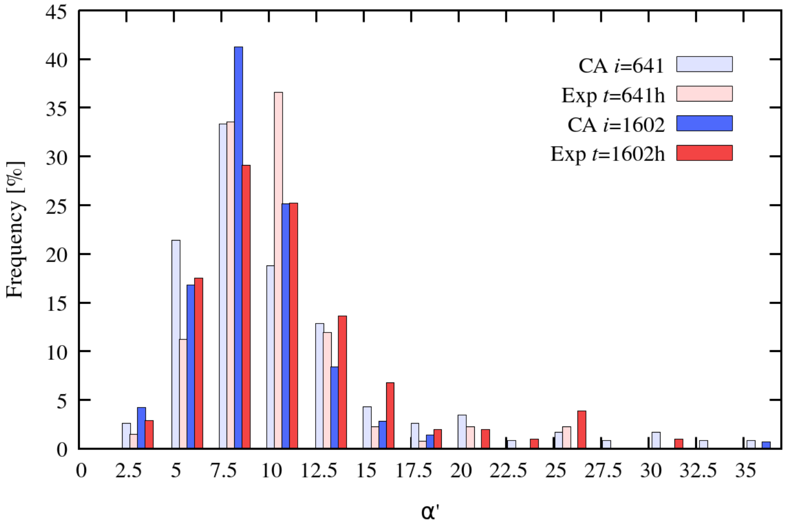

Figure 16: Comparison of experimental (in pink and red) and CA simulated (light-blue and blue) histogram distributions of groove angles at different time steps, t=641 h and t=1602 h, and at corresponding CA iterations. For each set of bars, α' values are referred to the α' interval defined by the values in the abscissa inside which they are represented.

2D sections and are therefore larger than the corresponding α 3D angles, as discussed in [29].

Table 4: Comparison between experiments and simulations in terms of average alpha and standard deviation at two different time steps

Parameter	Experimental tests [7]		CA simulations	
	t = 641 h	t = 1602 h	i = 641	i = 1602
Average alpha	11.6°	11.5°	10.9°	9.9°
Standard deviation	6.2°	5.1°	3.8°	3.6°

5.2. *Mass loss kinetics*

Figure 17 shows the comparison between simulations and experiments, in terms of *ETL* and *CR*. CA simulation results have been scaled with the above-mentioned space and time factors. The equivalent thickness loss has been divided in two components: the ETL due to the material dissolution (represented in black) and the one due to grain dropping (difference between the red squared points and the black curve). This distinction is not possible in the experiments.

In order to match the definitions that were used in [7], the following corresponding definitions are considered

$$ETL_{sim}\left(t\right) = \frac{N_{mat}\left(0\right) - N_{mat}\left(t\right)}{N_{xy}} A \tag{11}$$

where $N_{mat}\left(t\right)$ is the sum of the number of IGN and GRN cells at time t, N_{XY} is the number of grid cells in a XY-plane and A is the space scaling factor. Note that, as the horizontal axis are now plotted in real time, iteration i can be replaced with time t, as $B = 1$.

The corrosion rate is defined by

$$CR_{sim}\left(t + \frac{\Delta t}{2}\right) = \frac{ETL_{sim}\left(t + \Delta t\right) - ETL_{sim}\left(t\right)}{\Delta t} \times \frac{8760}{B} \tag{12}$$

where Δt is chosen equal to 160 (a time interval large enough to average corrosion rates), the factor 8760 is introduced again to have standard corrosion rates in μm/y.

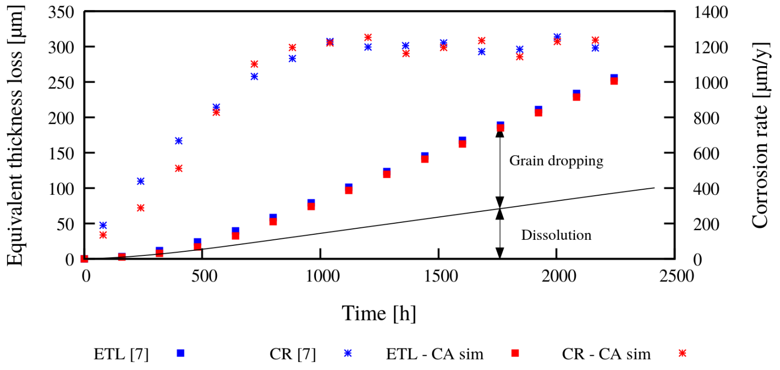

Figure 17: Weight loss comparison between CA simulations (in red) and experimental tests (in blue). The black line represents the portion of equivalent thickness loss that comes from the material dissolution.

The 3D CA model shows a good agreement with the experimental tests. At the beginning, the corrosion rate grows linearly with time while the equivalent thickness loss squarely evolves with it. Then, a transition regime is observed between 600 h and 1000 h. After t=1000 h, the corrosion rate becomes constant and the weight loss increases linearly with time. This behaviour is related to the morphology of the system. Firstly, grooves are formed and progress into the material, causing a progressive grain detachment. Then, grains start dropping with a certain periodicity (depending on the size). On average, when the first grain layer is detached, a stationary corrosion rate is reached.

5.3. Evolution of the surface morphology

The considerations on the mass loss discussed in the previous paragraph give only a mean information of the degradation of the SS in terms of mean thickness loss. However, taking into account the localized character of IGC, the corrosion is deeper in some locations of the SS like at the bottom of the grooves, as illustrated in Figure 2 and Figure 14. As these points define the residual available thickness of SS, it is fundamental to have information on their time-dependent position. However, information on the deepest corrosion is experimentally only accessible through analysis of 2D cross sections (Figure 2) which destroy the material.

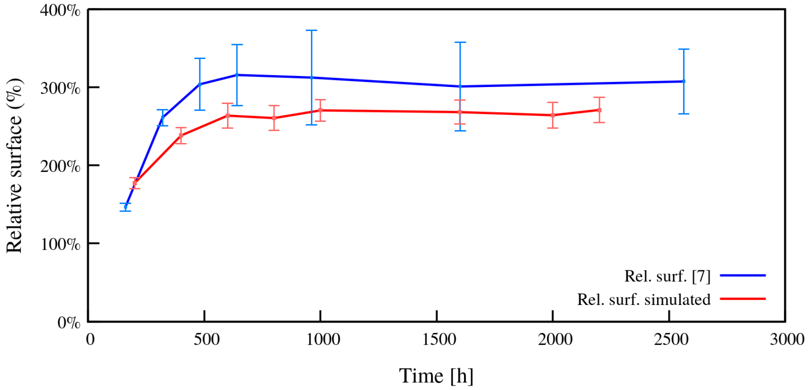

Figure 18: Comparison of the relative surface with experimental results in blue and simulated results in red. The error bars are estimated at $2\sigma/\sqrt{Z}$, where σ is the standard deviation and Z is the number of tests.

The evolution of the relative corrosion surface gives a first set of information on this aspect. It is defined as the ratio of the corroded surface at time t to the corresponding initial planar surface. In practice it can be calculated from 2D cross section pictures, as the ratio of the contours of the corroded surface to their horizontal projection. A comparison between numerical and experimental results is given in Fig. 18. The numerical results were obtained by averaging over four equally spaced cross sections and ten Voronoï structures.

Both curves present a similar trend. The relative surface evolution starts with a transitory regime up to around t=500 h; then the stationary regime starts. Once again, the trend of this parameter reflects the two corrosion regimes: groove progression (transitory) and grain detachment (stationary). CA results are comparable with experimental ones. The differences between the two curves is within the error bars.

5.4. Evolution of the distribution of the deepest penetrations

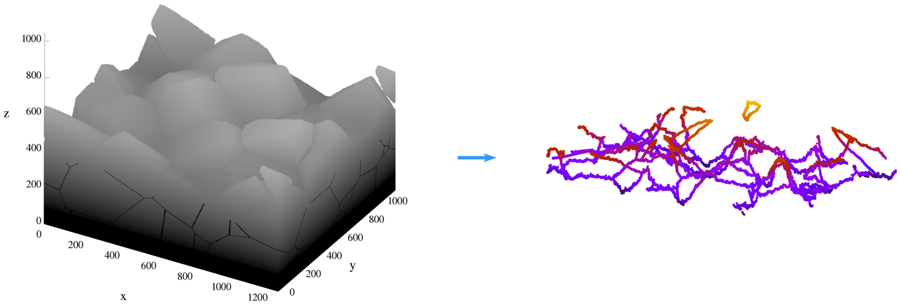

Figure 19: Representation of the grain boundary - solution interface during corrosion.

At a given corrosion time, the spatial distribution of the deepest points of the grooves corresponds to the spatial distribution of the grain boundary cells that are in contact with the solution (IGN-SOL). An example of an IGN-SOL interface is presented in Figure 19. It should be noted that the synchronous algorithm adopted in [19] for $P_{ign} = 1$ showed a homogeneous dissolution of IGN with the lowest points at identical height. The present asynchronous algorithm is more satisfactory in this case, since it shows a distribution of such points similar to experimental observations.

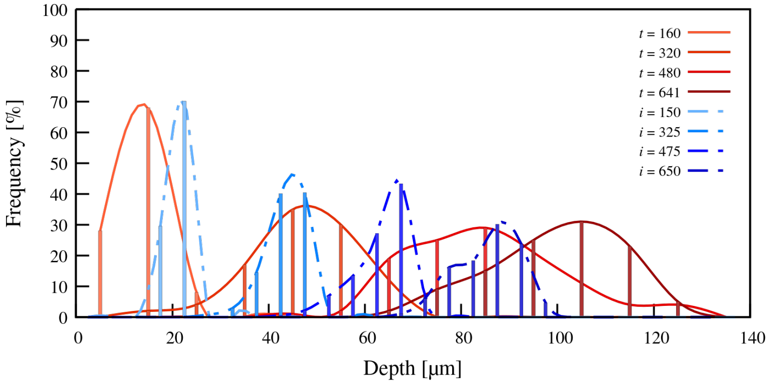

Figure 20: IGN-SOL spatial distribution as a function of the depth for experimental results (red shades) et CA simulations (blue shades). Lines are provided as guides.

The IGN-SOL spatial distribution has been calculated every 25 simulation steps for the different Voronoï structures. The distributions present a Gaussian-type pattern, as shown in Figure 20. It differs slightly from a perfect "bell curve" since the corrosion algorithm involves non-independent events. The two approaches show the same trend, although their definition is slightly different. CA simulations consider, at each (x,y) coordinate, the lowest IGN cell that is in contact with a SOL cell, while experiments consider only the lowest points of the grain boundary grooves. At low depth, a narrow peak is present; then, as the depth increases, the number of non-independent events increases and the distribution spreads. When the first grain characteristic dimension is reached on average in terms of depth and grain detachment starts, a small hump appears aside the main distribution peak.

The evolution of the IGN-SOL interface depth as a function of time is presented in Figure 21. The three curves represent respectively the minimum (in red), the average (in blue) and the maximum (in black) depths, estimated every 25 simulations (which correspond to 25 hours). The average and the maximum

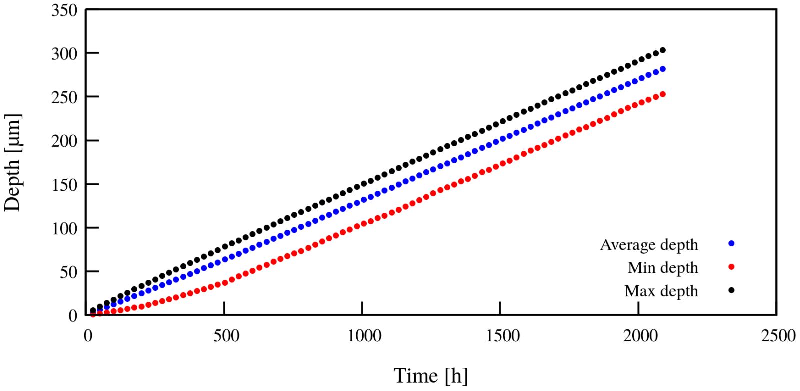

Figure 21: Representation of the average IGN-SOL interface depth as a function of time. Results are calculated every 25 simulation steps.

interface depths present a linear trend. The minimum interface depth presents instead a linear trend up to 500 h, then it switches to another linear trend with a slightly higher slope. This particular behaviour is again linked to the two regimes that characterize the IGC phenomenon. These data have a high industrial interest, since they give important information on when a material may reach a critical failure point in terms of corrosion.

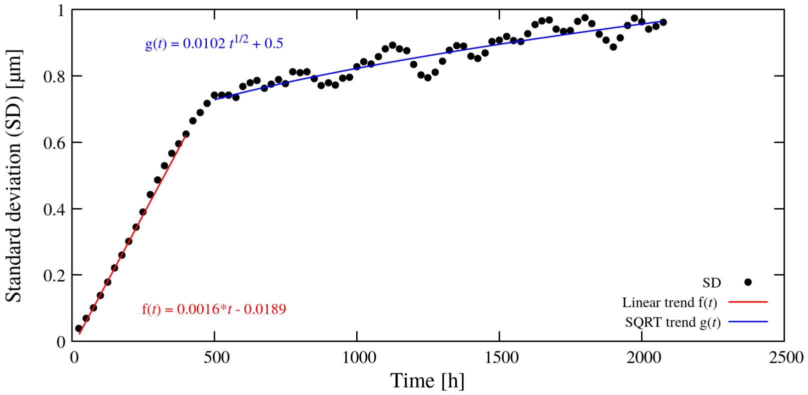

Figure 22: Representation of the standard deviation of the IGN-SOL spatial distribution as a function of time.

The time evolution of the standard deviation (SD) of the IGN-SOL interface depth distribution is shown in Figure 22. At first, it seems to follow a linear trend; then it switches to a square-root-of-time trend. The two trends correspond to the two morphological regimes that characterize the IGC, as seen in Figure 20. The linear regime matches with the groove progression inside the material, while the second one reflects the combination of the previous effect together with grain detachment. Due to the limited dimensions of the simulated systems, the grain detachment events have a large impact on the corrosion progression and explain the oscillations at $t > 1000$ h.

CA modelling has been used as a so called grey box approach. Like for all simulations, it is necessary to introduce in the simulation the real space and time scales. For the space, the relation between grain size and number of cells is chosen. There is no unique choice: a "best choice" is made to sufficiently balance a detailed description (large lattice) and the simulation time (not too large lattice). The time scale is then derived from a velocity ratio using the stationary IGC velocity as reliable physical quantity, as it is obtained as an average over several points. Finally, the grain corrosion velocity is taken from the experimental study. It should be noted that, as a grey box approach, the method cannot predict corrosion rates, but it uses coefficients provided experimentally.

However, by only using three input numbers (two of them (A and B) are necessary to give a meaning to the simulation) several results (in the form of trends or graphs) are obtained. The main results are listed below.

- The model reproduces several IGC features that are compared to experimental results of [7]:
  - the Voronoï tessellation reasonably accounts for the material morphology;
  - the approach shows the characteristic grooves expected for "non-sensitized" SS IGC corrosion;
  - the simulation provides the angular distribution of the grooves;

  - the ETL and corrosion velocity curves are well reproduced and exhibit the two characteristic corrosion kinetic regimes;
  - the relative surface morphology is also reproduced.

- New features are obtained:
  - information about grain dropping and pure granular dissolution have been separated;
  - lowest corrosion point depth distribution histogram is traced;
  - supplementary information of minimum and maximum of these points and their standard deviation have been obtained.

Note that some features are difficult to obtain experimentally as they concern the bulk material and require the physical destruction of the sample as they cannot be performed in situ.

6. Conclusion

In this paper, a 3D cellular automata model is proposed to investigate the IGC phenomenon. The model provides realistic morphological characteristics of IGC like groove shaped corrosion, grain detachment. The model can be considered as a grey box approach. The approach feeds on experimental parameters and combines them with mechanistic features within the CA approach. Here, corrosion velocities are used to parametrize the corrosion probabilities of the model. In contrast with [19, 31], a new asynchronous algorithm has been used which ensures linearity between CA parameters and real corrosion kinetics. This is useful to treat IGC modelling which involves different corrosion kinetics for granular and intergranular material.

Concerning the quantitative comparison, a particular attention has been spent to validate the choice of the CA grid. The model can thus provide quantitative kinetics of the ETL and angular distribution of the grooves. The model also gives new insights on IGC as it is able to separate the contributions from granular and intergranular corrosion and gives the statistical spatial distribution of the penetration depths of the corrosion. The precise knowledge of this distribution is of critical interest for managing intergranular corrosion of SS in industry. These features help characterizing the material dissolution and assess system reliability predictions.

This article shows how to pass from experimental to simulation quantities. The model is simple and draws input parameters directly from phenomenological corrosion velocities. However, finer mechanistic descriptions can be considered in the future. For instance, the corrosion probabilities can be based on intrinsic quantities like energetic barriers and allow taking into account temperature effects. A detailed description of the environment can also be examined. In this model, a simplified effect of the strength of the solution is introduced by connecting the corrosion probability to the amount of solution surrounding a corroded cell. In the future, it will also be possible to account for diffusion and concentration effects of corrosive compounds in solution.

Acknowledgements

The authors would like to thank Damien Féron for his useful comments on this paper, and the CEA and the National Graduate School of Chemistry in Paris for supporting this work.

Data availability

The raw/processed data required to reproduce these findings cannot be shared at this time as the data also form part of an ongoing study.

Table 5: List of symbols

t, Δt	time, time duration in experiments in hours h
i, Δi	iteration, number of iterations in the simulation
$m(t)$	experimental cumulated mass loss as a function of t in g
ρ	SS density in g.cm^{-3}
S	initial surface of polished sample in cm^2
D_{exp}, D_{sim}	characteristic size of grains for experiments in μm and for simulations in number of cells
$ETL_{exp}(t), ETL_{sim}(i)$	equivalent thickness loss as a function of time t for experiments and iterations i for simulations
$CR_{exp}(t)$, $CR_{sim}(i)$	corrosion velocity as a function of time t for experiments and iterations i for simulations
$v_{ign}(t), v_{ign}(i)$	grain boundary corrosion rate (corresponding to V_{gb} in article [7]) as a function of time t for experiments and iterations i for simulations
$v_{grn}(t), v_{grn}(i)$	grain corrosion rate (V_s in article [7]) as a function of time t for experiments and iterations i for simulations
α, β	groove angles see Figure 4 in degrees °
H'^*	groove depth see Figure 4
N_X, N_Y, N_Z	dimensions of the system in the CA simulations in number of cells
N_b	number of SOL neighbours to a cell
$N_{b,max}$	maximum number of neighbours to a cell, 12 for HCP lattice
P_{grn}	corrosion probability for grain corrosion
P_{ign}	corrosion probability for intergranular corrosion
$v_{grn}^{stat}(P_{grn})$	stationary corrosion velocity of grains as a function of grain corrosion probability
$\lambda^{stat}(P_{grn})$	stationary chemical roughness as a function of grain corrosion probability
N_{grn}	number of grain cells (GRN) in the system
N_{mat}	number of grain (GRN) and intergranular (IGN) cells in the system
$N_{grn-sol}$	number of grain cells in contact with at least a SOL cell
N_{seed}	number of seeds used to obtain the Voronoï structure

Table 6: List of abbreviations

PUREX: Plutonium and Uranium Refining by Extraction
IGC: intergranular corrosion
WL: weight-loss
SROM: stochastic reduced order model
SS: stainless steel
AISI: American Iron and Steel Institute
GB: grain boundaries
HCP: hexagonal close-packed grid
CA: cellular automata
Cellular automata type of cells: *SOL* solution, *GRN* grain, *IGN* intergranular cells
CUDA: Compute Unified Device Architecture

References

[1] P. Fauvet, Corrosion issues in nuclear fuel reprocessing plants, Elsevier Ltd, 2012. `doi:10.1533/9780857095343.5.679`.

[2] G. Andreoletti, P. Chambrette, A. Mercier, J.-P. Moulin, F. Thurin, C. Vittoz, Industrial feedback of intercycle uranyl nitrate concentration in stainless steel 304L evaporator, Eurocorr 2006, Maastricht, the Netherland (2006).

[3] F. Ueno, C. Kato, T. Motooka, S. Ichikaway, M. Yamamoto, Corrosion phenomenon of stainless steel in boiling nitric acid solution using large-scale mock-up of reduced pressurized evaporator, Journal of Nuclear Science and Technology 45 (10) (2008) 1091–1097. `doi:10.1080/18811248.2008.9711897`.

[4] S. Zhao, D. A. Wolfe, T.-S. Huang, G. S. Frankel, Generalized model for

IGC growth in aluminum alloys, Journal of Statistical Planning and Inference 137 (7) (2007) 2405–2412. `doi:10.1016/j.jspi.2006.09.021`.

[5] M. L. C. Lim, R. G. Kelly, J. R. Scully, Overview of intergranular corrosion mechanisms, phenomenological observations, and modeling of AA5083, Corrosion 72 (2) (2016) 198–220. `doi:10.5006/1818`.

[6] S. Sarkar, J. E. Warner, W. Aquino, M. D. Grigoriu, Stochastic reduced order models for uncertainty quantification of intergranular corrosion rates, Corrosion Science 80 (2014) 257–268. `doi:10.1016/j.corsci.2013.11.032`.

[7] B. Gwinner, M. Auroy, F. Balbaud-Célérier, P. Fauvet, N. Larabi-Gruet, P. Laghoutaris, R. Robin, Towards a reliable determination of the intergranular corrosion rate of austenitic stainless steel in oxidizing media, Corrosion Science 107 (2016) 60–75. `doi:10.1016/j.corsci.2016.02.020`.

[8] E. Tcharkhtchi-Gillard, M. Benoit, P. Clavier, B. Gwinner, F. Miserque, V. Vivier, Kinetics of the oxidation of stainless steel in hot and concentrated nitric acid in the passive and transpassive domains, Corrosion Science 107 (2016) 182–192. `doi:10.1016/j.corsci.2016.02.031`.

[9] G. O. H. Whillock, B. F. Dunnett, Intergranular corrosion testing of austenitic stainless steels in nitric acid solutions, presented at the Eurocorr 2004, Société de Chimie Industrielle, Paris (France) (2004) 1–10.

[10] Standard Test Method for Conducting Cyclic Potentiodynamic Polarization Measurements for Localized Corrosion Susceptibility of Iron-, Nickel-, or Cobalt-Based Alloys, ASTM G61 (2018).

[11] Standard Test Method for Electrochemical Reactivation (EPR) for Detecting Sensitization of AISI Type 304 and 304L Stainless Steels, ASTM G108 (2015).

[12] M. Orazem, B. Tribollet, Electrochemical Impedance Spectroscopy, 2nd Edition, Wiley-Interscience, 2017.

[13] S. Ningshen, M. Sakairi, Corrosion degradation of AISI type 304l stainless steel for application in nuclear reprocessing plant, Journal of Solid State Electrochemistry 19 (12) (2015) 3533–3542. `doi:10.1007/s10008-015-2891-y`.

[14] E. F. Diaz, C. Cuevas-Arteaga, N. Flores-García, S. Mejía Sintillo, O. Sotelo-Mazón, Corrosion performance of AISI-309 exposed to molten salts V_2O_5 - Na_2SO_4 at 700°C applying EIS and R p electrochemical techniques, Journal of Spectroscopy 2015 (2015) 1–12. `doi:10.1155/2015/826759`.

[15] J. S. Armijo, Intergranular corrosion of nonsensitized austenitic stainless steels, Corrosion 24 (1968) 24–30.

[16] W. D. Callister, Materials science and engineering: an introduction, 7th Edition, John Wiley & Sons, 2007.

[17] C. Singh, H. Kumar, R. Kumar, Research on the diffusion of ti-based stabilizer through flux coated GTAW to reduce carbide precipitation in SS304 weldment, Materials Today: Proceedings 5 (9) (2018) 18689–18696.

[18] K. E. Pinnow, A. Moskowitz, Corrosion resistance of stainless steel weldments, Weld J. 49 (6) (1970) 278–284.

[19] D. di Caprio, J. Stafiej, G. Luciano, L. Arurault, 3D cellular automata simulations of intra and intergranular corrosion, Corrosion Science 112 (2016) 438–450. `doi:10.1016/j.corsci.2016.07.028`.

[20] C. F. Pérez-Brokate, D. di Caprio, E. Mahé, D. Féron, J. de Lamare, Cyclic voltammetry simulations with cellular automata, Journal of Computational Science 11 (2015) 269–278. `doi:10.1016/j.jocs.2015.08.005`.

[21] B. Chopard, M. Droz, Cellular Automata Modeling of Physical Systems, Cambridge University Press, 1998.

[22] P. Cordoba-Torres, K. Bar-Eli, V. Fairen, Non-diffusive spatial segregation of surface reactants in corrosion simulations, Journal of Electroanalytical Chemistry 571 (2) (2004) 189–200. `doi:10.1016/j.jelechem.2004.05.009`.

[23] S. Lishchuk, R. Akid, K. Worden, J. Michalski, A cellular automaton model for predicting intergranular corrosion, Corrosion Science 53 (2011) 2518–2526. `doi:10.1016/j.corsci.2011.04.027`.

[24] S. Lishchuk, R. Akid, K. Worden, Model-based prognosis for intergranular corrosion, in: Proceedings of the 4th European Workshop on Structural Health Monitoring, 2008, pp. 340–348.

[25] K. Jahns, K. Balinski, M. Landwehr, V. B. Trindade, J. Wubbelmann, U. Krupp, Modeling of intergranular oxidation by the cellular automata approach, Oxidation of Metals 87 (3) (2017) 285–295. `doi:10.1007/s11085-017-9732-6`.

[26] T. Igarashi, A. Komatsu, T. Motooka, F. Ueno, Y. Kaji, M. Yamamoto, Simulations of intergranular corrosion feature for stainless steel using cellular automata method, Zairyo to Kankyo/ Corrosion Engineering 63 (7) (2014) 431–437. `doi:10.3323/jcorr.63.431`.

[27] F. Ueno, A. Komatsu, T. Igarashi, M. Yamamoto, Study of the effect of phosphorus concentration on intergranular corrosion of stainless steel in boiling nitric acid solution, in: Eurocorr Pisa (Italy), 2014.

[28] A. Taleb, J. Stafiej, Numerical simulation of the effect of grain size on corrosion processes: Surface roughness oscillation and cluster detachment, Corrosion Science 53 (8) (2011-08) 2508–2513. `doi:10.1016/j.corsci.2011.04.008`.

[29] B. Gwinner, J.-M. Borgard, E. Dumonteil, A. Zoia, A stereological approach for measuring the groove angles of intergranular corrosion, Corrosion Science 115 (2017) 1–7. `doi:10.1016/j.corsci.2016.11.005`.

[30] L. Beaunier, M. Froment, C. Vignaud, A kinetical model for the electrochemical grooving of grain boundaries, Electrochimica Acta 25 (10) (1980) 1239–1246.

[31] S. Guiso, D. di Caprio, J. de Lamare, B. Gwinner, Influence of the grid cell geometry on 3D cellular automata behavior in intergranular corrosion, Submitted to Journal of Computational Science.

[32] A. Okabe, A. Suzuki, Locational optimization problems solved through voronoi diagrams, European Journal of Operational Research 98 (3) (1997) 445–456. `doi:10.1016/S0377-2217(97)80001-X`.

[33] G. Voronoi, Nouvelles applications des paramètres continus la théorie des formes quadratiques. deuxième mémoire, recherches sur les parallélloèdres primitifs", Journal für die Reine und Angewandte Mathematik 134 (1908) 198–287.